Chapter 3

Multifragmentation in nearly symmetric and asymmetric reactions: A detailed study and comparison with experimental measurements

3.1 Introduction

Nuclear multifragmentation is one of the most important reaction mechanisms observed in a reaction at intermediate energies [4, 20–22, 59, 75]. At low incident energies, fusion-fission dominates the physics, whereas, frequent violent nucleon-nucleon binary collisions at higher incident energies disassemble the colliding nuclei completely. Though, the multiplicity of various fragments increases with excitation energy, a rise and fall can, however, be seen when intermediate mass fragments are considered exclusively [22, 92, 122, 125, 137, 138, 242]. In addition, when charge (or mass) yields of fragments were fitted with exponential/power law $\propto e^{-\lambda Z_f}/Z_f^{-\tau}$ (or $e^{-\lambda A_f}/A_f^{-\tau}$), a minimum (which is associated with the onset of multifragmentation) was reported in λ/τ with respect to incident energy [119, 121, 231, 243].

On the theoretical front, multifragmentation can be studied using statistical [4, 73, 150, 151, 153–155] as well as dynamical models [35, 148, 149, 169, 171–174, 176, 177, 179, 180, 182–187, 189]. At the same time, with recent advances in the radioactive ion beam technology, isospin degree of freedom has also been incorporated in theoretical approaches [186, 187, 189] and thus, provides greater insight about the reaction dynamics. Inter-

estingly, the studies of the charge (or mass) yields with incident energy using isospin-dependent quantum molecular dynamics model remains to be very rare [158].

Further, it is worth mentioning that most of the attempts for multifragmentation were limited to symmetric colliding partners only [22, 87, 95, 118, 125, 231, 240, 244, 245] few others, however, were extended to the collisions of asymmetric projectile-target combinations [92, 122, 137, 138, 158, 243, 246–249]. The asymmetry of a reaction is given by asymmetry parameter η, where $\eta = [(A_T\text{-}A_P)/(A_T+A_P)]$; $A_{P/T}$ = mass of the projectile/target. One should keep in mind that the dynamics of asymmetric reactions can be quite different than that of symmetric reactions. Whereas, the excitation energy is stored in the form of compressional energy in the latter, the former has a significant share in terms of thermal energy. In this regard, reactions of $^{16}_{8}$O/$^{40}_{18}$Ar/$^{84}_{36}$Kr+AgBr and $^{197}_{79}$Au + $^{197}_{79}$Au were studied using different versions of molecular dynamics approach given by Donangelo *et al.* [249]. Their findings revealed that these approaches successfully explain the intermediate mass fragments (IMFs) multiplicities for the reaction of $^{197}_{79}$Au + $^{197}_{79}$Au (symmetric reactions), in contrary, they fail to reproduce the measured multiplicities in asymmetric reactions. However, the implementation of the Pauli-potential in molecular dynamics approach decreases the discrepancy between theoretical results and measured multiplicities [249]. The above failure was attributed to the improper treatment of the thermodynamical properties in dynamical approaches. Another study was performed in Ref. [250] where transition from the fusion-fission to multifragmentation in the collisions of $^{16}_{8}$O + $^{80}_{35}$Br was investigated using quantum molecular dynamics model. There also, significant influence of the Pauli-potential and damping procedure was found on the multiplicities of free nucleons (FNs), light charged particles (LCPs) as well as intermediate mass fragments (IMFs); especially at low incident energy. Similar inadequacy of the molecular dynamics approach was also reported by Peaslee *et al.* [138] while investigating the reaction of $^{84}_{36}$Kr + $^{197}_{79}$Au at lower incident energies. Though, this is true for the Quantum Molecular Dynamics (QMD) model, the Isospin-dependent Quantum Molecular Dynamics (IQMD) model has additional repulsion due to symmetry potential, isospin dependence of the nucleon-nucleon cross-section as well as initial larger Fermi-momentum (as discussed in the Chapter 2). In addition, this model also has improved Pauli-blocking mechanism compared to the QMD model. Therefore, it would be interesting to see the behavior of the IQMD model (with these refined ingredients) towards the dynamics of asymmetric reactions where most of the dynamical approaches fail to explain

the measurements. The aim of present analysis, therefore, is to study the dynamics of asymmetric reactions using the IQMD model and to have a comparison with other model calculations, wherever available. It should be noted that asymmetric collisions have also been studied with ALADiN spectrometer [137, 251] at higher incident energies till few GeV/nucleon but in the present study, we restrict ourselves to lower incident energies up to 400 MeV/nucleon. Before presenting the results, it is important to describe some of the experimental facilities (which are equally important as they have been serving the nuclear physics community with the useful experimental data) with their contribution to the development of the nuclear physics.

3.2 Details of key experimental facilities

Besides the many radioactive ion beam facilities that already exist in the world, a number of next-generation radioactive ion beam facilities are being constructed or planned (see Chapter 1 for the details). At these facilities, nuclear reactions involving nuclei with a large neutron or proton excess can be studied, thus providing a great opportunity to study both the structure of rare isotopes and the properties of hot and dense nuclear matter. As mentioned in Chapter 1, a large number of experimental facilities have been established so far and the measurements using these facilities provide a satisfactory analysis of the multifragmentation over wide range of mass, incident energy and colliding geometry. Among all the mentioned collaborations/facilities, the research program of various collaborations/facilities such as FOPI, INDRA, ALADiN and MSU 4π array is mainly focused on the process of collective flow and multifragmentation. In the present thesis, we will also compare our theoretical results with the measurements reported by these collaborations/facilities. Therefore, next we will discuss these collaborations/facilities in detail.

3.2.1 FOPI detector

As stated in the Chapter 1, the main tool at GSI in Germany is the heavy-ion accelerator facility. This facility consists of Universal Linear Accelerator, UNILAC (energy of 2 - 11.4 MeV/nucleon), the heavy-ion- Synchroton (0.01 - 2 GeV/nucleon) and Experimental Storage Ring, ESR (0.005 - 0.5 GeV/nucleon) etc. The UNILAC was commissioned in 1975 and later on, developments have been made to boost the ion acceleration from 10%

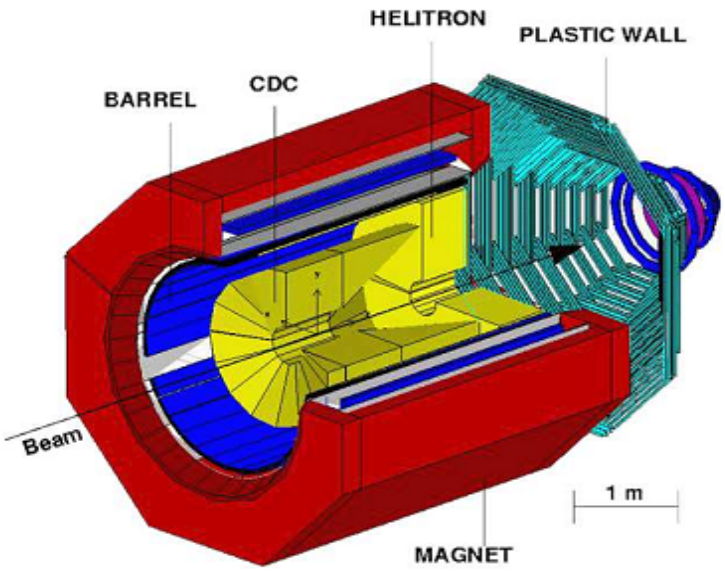

Figure 3.1: FOPI detector with indication of sub-detectors. The figure is taken from Ref. [254].

of light speed to 90%.

The FOPI (FOur PI) detector at GSI is being used to investigate the properties of hot and dense nuclear matter since 1990 [252, 253]. A schematic view of the detector is shown in Fig. 3.1. With the help of various sub-detector components [252, 253], the FOPI detector at GSI covers nearly full solid angle (4π). The complete installment of the FOPI detector was passed through three stages: (i) The first stage was completed in 1990. This phase consists of forward Plastic Wall (PW) and an inner shell of 188 energy loss detectors. The wall measured the charge and velocity of all charged particles emitted with laboratory polar angles between $1^\circ < \Theta_{Lab} < 30^\circ$ over the full azimuthal; (ii) the second phase was completed in 1992 and it consists of the installation of *Superconducting Magnet* (SM) and *Central Drift Chamber* (CDC). This enabled momentum determination of charged particles within an expanded angular range of $30^\circ < \Theta_{Lab} < 150^\circ$ and (iii) in the final phase (completed in the beginning of 1995), the *Scintillator* and *Cherenkov*

Barrel and the forward *drift chamber Helitron* were installed to determine the velocity and also permit momentum determination down to $\Theta_{Lab} < 70°$. In the FOPI detector, the *Start system* is used to count incoming ions and provides the reference time t_0 to all sub-detectors. The anti-coincidence veto system can reject the beams, which are not focussed on the target. The *Superconducting magnet* (having length and diameter are 3.3 m and 2.4 m, respectively) gives a homogenous solenoidal magnetic field of 0.6 Tesla parallel to the beam axis. The CDC, *Helitron* and *Barrel* are placed inside the magnet as shown in Fig. 3.1. The strong solenoid magnetic field helps in the measurement of transverse and total momentum of the charged particles. The CDC is the main tracking system of the FOPI detector. It has cylindrical shape with conical end caps at the front and back side and it has the full azimuthal coverage and the polar acceptance covered from 33° to 145°. The CDC is made up of 16 sub-detectors and each sub-detector further consists of 60 *Sense* and 61 *Potential* wires parallel to the beam axis. During the process of charged particles passing through the CDC gas volume, the ionized electrons drift towards the *Sense* wires, where the signals are collected. Also, in the FOPI detector, there is a *Drift Chamber* that helps to track the charged particles in the forward region. This chamber covers the full azimuthal angles and the polar angles from 7° to 30° in the laboratory frame. The other part of the FOPI detector i.e., *Barrel* consists of 180 plastic scintillators and the geometrical matching between the tracks of the CDC and hits in the *Barrel* is required to improve the particle identification with certain matching condition. The *Plastic wall* (also called PLAWA) is made up of 512 *scintillator strips* and it provides very fast information of the charged particle multiplicity in a given event, thus, it is suited for the online trigger. The ZDC (Zero-Degree-Counter) measures the time-of-flight, the velocity and the energy loss of the charged particles.

3.2.2 INDRA detector

The 4π-multidetector INDRA (Identification de Noyaux et Detection avec Resolution Array) was constructed in 1989 at GANIL in France and it offers high capabilities for the simultaneous detection of the numerous light charged particles and fragments that are emitted during heavy-ion collisions. A total of 640 individual detectors cover 90% of the 4π solid angle. The detector operated under vacuum is axially symmetric and segmented in 336 independent cells allowing efficient detection of high multiplicity events. In order to handle problems of designing such a complex 4π-detector, the complete mechanics of

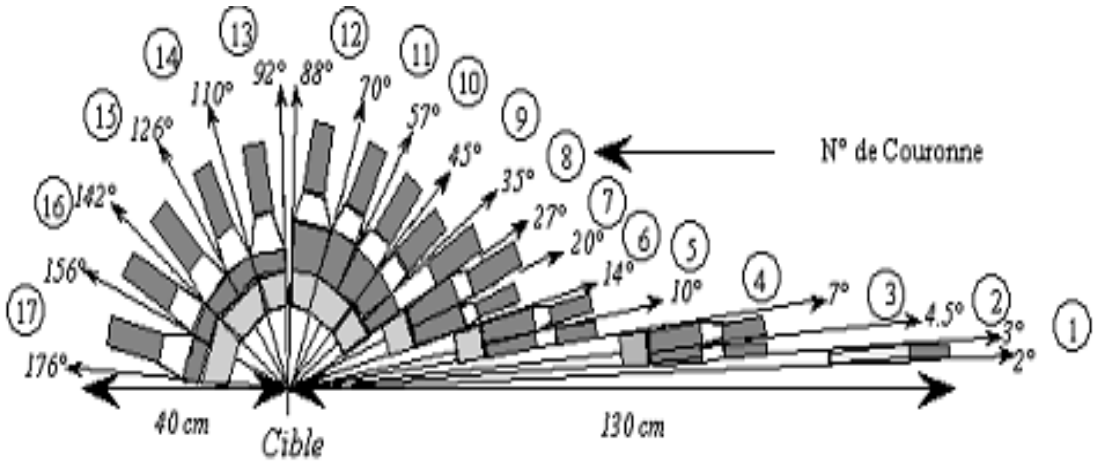

Figure 3.2: Geometrical outline of the INDRA detector (cut along the beam axis). The detectors are arranged in beam axis. "Reprinted from Nuclear instruments and Methods in Physics Research A, **357**, J. Pouthas *et al.*, INDRA, a 4π charged product detection array at GANIL, 418-442, Copyright (1995), with permission from Elsevier".

INDRA, including space required by electronics and connections was computer designed [255]. Nucleus identification at very low energy threshold (1 MeV/nucleon) is obtained by using ionization chambers; which operates in low pressure gas region. The combination of silicon (300 μm thick) and Cesium Iodide (5 to 14 cm in length) detectors is used to measure the residual energies. The fast counting *phoswich scintillator* (NE102/NE115) is used to cover very forward angles. The geometrical outline of the INDRA detector is shown in Fig. 3.2. This detector is divided into I7 rings that are coaxial and help to detect light charged particles. Ideally, a 4π detector should provide, on an event by event basis, the number of particles in the event and for each particle its identity (atomic number and mass), its energy (or velocity) and its emission angle. Moreover, the telescopes used in the INDRA detector have an intrinsic possibility of satisfying nucleus identification

and energy resolution requirements. The INDRA collaboration focuses on the study of collision dynamics via mid-rapidity emission, stopping, directed and elliptic flows and isospin-diffusion and multifragmentation of hot nuclei, multiparticle correlation functions as well as study of various entrance channel effects [66, 94, 108, 256] and hence, covers milestone achievements.

3.2.3 ALADiN spectrometer

ALADiN (A large Acceptance Dipole magNetis) an experimental collaboration which uses ALADiN spectrometer to perform experiments and hence, probes the properties of the hot and dense nuclear matter [92, 140, 248, 258–261]. To study the mass and isospin effects on the matter produced during the breakup of projectile spectators as well as to cover different combinations of masses and neutron-proton ratios, an experiment was performed by ALADiN collaboration taking four different projectiles ($^{107}_{50}$Sn, $^{124}_{50}$Sn, $^{124}_{57}$La and $^{197}_{79}$Au) with an incident energy of 600 MeV/nucleon. The two later beams have been delivered by the *FRagment Spectator* (FRS) of the GSI as products of the fragmentation of primary $^{142}_{60}$Nd beam at 1.1 GeV/nucleon on $^{9}_{4}$Be production target. A cross-sectional view of the setup is shown in Fig. 3.3. The isotopic composition of the secondary beams was determined and monitored from the magnetic rigidity measured at the FRS, from a velocity measurement along the 80-m flight path between the FRS and the ALADiN setup, and from the charge measurement with the TP-MUSIC IV detector. Projectile fragments entering into the acceptance of the magnet are tracked and identified in the TP-MUSIC IV detector and in the time-of-flight (TOF) wall. Neutrons emitted in directions close to $\Theta_{lab} = 0^{\circ}$ are detected with the Large-Area Neutron Detector (LAND). The dash-dotted lines represent the beam directions before and after the deflection by 7^0 in the field of the ALADiN magnet. The measurement of the charge and the momentum vector of all projectile fragments with $Z_f \geq 2$ has been performed with high efficiency and high resolution with the TP-MUSIC IV detector [262]. Using the reconstructed values for the momentum vector and path length, the charge of each particle measured by the TP-MUSIC detector, and the time of flight given by the TOF-wall, the mass of each detected charged particle can be calculated. A single mass resolution for charges up to 12 is obtained, corresponding to the mass resolution $\triangle$A/A of approximately 4.0% (FWHM) for light fragments. The details of the experimental setup are taken from the Refs. [262, 263] .

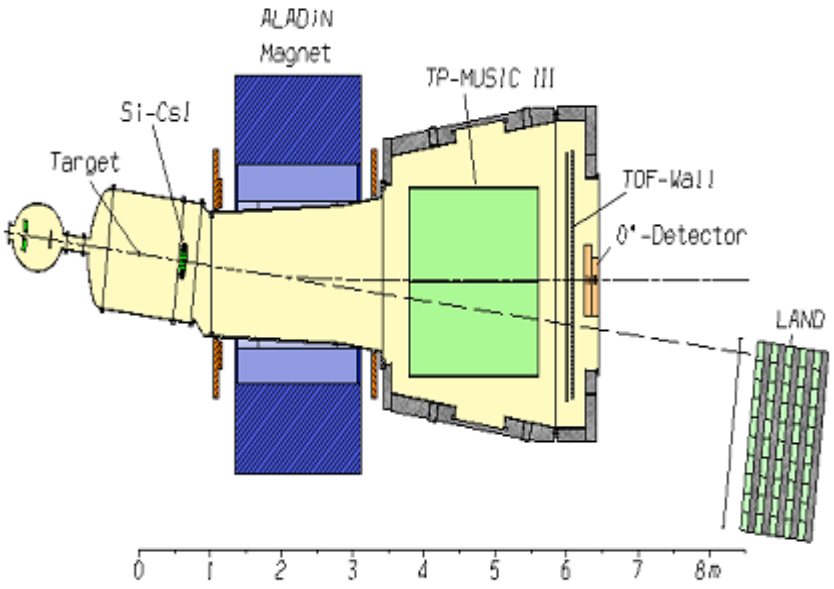

Figure 3.3: Cross-sectional view of the ALADiN setup. The figure is taken from the Ref. [257].

3.2.4 MSU 4π-array

A compact and highly granular particle detection array, covering almost 90% of 4π in solid angle was established at National Superconducting Cyclotron Laboratory (NSCL) in Michigan State University (MSU) of USA. This 4π-array is composed of 30 discrete sub-modules enfolded within a 32-faced, aluminium truncated icosahedron [264]. Its external structure looks like a soccer ball which is made up of 20 hexagonal and 12 pentagonal faces. All of the hexagonal faces along with 10 of the pentagonal faces act as black plates and 30 modules are placed upon them whereas, the left two pentagonal faces act as an entrance and exit for the incident beam. Each pentagonal (hexagonal) module is made of 5(6) close packed plastic phoswich detectors and a gas chamber is installed in front of each phoswich. This gas chamber can serve the purpose of ΔE detector for particles stopping in

the thin layer of the phoswich detector and as a standalone Bragg Curve Counter (BCC). The sub-division of BCC in the 5 most forward modules results into 6 separate detectors. A low pressure multi-wire proportional counter (MWPC) is placed in front of each BCC to detect the slow moving heavy fragments (the term "slow" and "fast" deal with the response time of the plastic-Ball when pierced by an energetic charged particles). To get more details of this 4π-array as well as its pictorial view, reader is referred to Ref. [264].

It is worth mentioning that we have performed bulk of calculations using IQMD model and our theoretical results are compared with the measurements of these 4π arrays in next sections.

3.3 Results and discussions

For the present study, we simulated several thousands events for the nearly symmetric reactions of $^{40}_{18}$Ar + $^{45}_{21}$Sc and $^{129}_{54}$Xe + $^{120}_{50}$Sn and asymmetric reactions of $^{84}_{36}$Kr + $^{197}_{79}$Au, $^{16}_{8}$O + $^{80}_{35}$Br, $^{16}_{8}$O + $^{108}_{47}$Ag, $^{129}_{54}$Xe + $^{197}_{79}$Au, $^{197}_{79}$Au + $^{12}_{6}$C, $^{40}_{18}$Ar + $^{64}_{29}$Cu, $^{40}_{18}$Ar + $^{108}_{47}$Ag, $^{36}_{18}$Ar + $^{197}_{79}$Au, $^{40}_{18}$Ar + $^{197}_{79}$Au, $^{197}_{79}$Au + $^{64}_{29}$Cu at different incident energies and colliding geometries. Note that the choice of beam energies is made as per available experimental measurements [75, 94, 97, 121, 122, 138, 175, 265–268]. We here use a soft equation of state supplemented by the energy-dependent nucleon-nucleon cross-section reduced by 20%, i.e, $\sigma_{NN} = 0.8\ \sigma_{NN}^{free}$. It is worth mentioning that the above reduction in the cross-section has been advocated by various earlier studies [269–276]. The reactions are followed till 300 fm/c where yields of various fragments gets saturated and binary collisions cease to exist at this stage. Further, it should be noted that centrality of the reactions, cuts in rapidity (wherever applied) and range of intermediate mass fragment's mass window (IMFs's mass range) for all the reactions have also been chosen as per measurements so as to impose experimental conditions as closely as possible. However, other cuts of energy threshold etc. could not be taken care of due to unavailability of complex filters. Before going to the description of the calculated results, we would like to mention that sometime, the need of supplementing the dynamical model calculations with statistical decay codes has been advocated in the literature [175]. For example, coupling with decay models was found to be essential where fine structure like odd-even effects are to be explained [277]. However, it has been shown in Ref. [278] that the statistical models have little effect on the charge distributions of fragments at central/semi-central collisions. On the other hand, statistical

models have to be taken into account for better description of fragment's distribution at peripheral collisions. Since, we have investigated the fragmentation of asymmetric reactions in nearly central and semi-central collisions and thus, we have not supplemented our calculations with any statistical code. Also, it is worth mentioning that studies do exist in the literature where comparisons of bare IQMD calculations with measured data (without any statistical code) have been presented for central/semi-central collisions [267, 268, 279, 280]. To have a clear picture, we have also calculated the approximate excitation energies of various fragments emitted in different mass asymmetric reactions. We found that lighter fragments have excitation energy of around 2 MeV/nucleon whereas, this excitation energy (at lower beam energies for mass asymmetric reactions) goes up to 3 MeV/nucleon for heavier fragments. In the present work, we study the dynamics of fragmentation for nearly symmetric as well as asymmetric reactions (covering a wide range of the asymmetry parameter η). So, let us first investigate the nearly symmetric reactions and after that we will come to the above mentioned asymmetric reactions.

3.3.1 Symmetric (or nearly symmetric) reactions

In Fig. 3.4, we display the calculated charge distributions for the central collisions of $^{40}_{18}$Ar + $^{45}_{21}$Sc at various bombarding energies. As stated above, the choice of centrality is as per experimental measurements. The available experimental data is also shown (see stars) and is extracted from Ref. [121]. Note that the data for the reaction of $^{40}_{18}$Ar + $^{45}_{21}$Sc was not available for incident energies of 20 and 30 MeV/nucleon. We have made these calculations for the completeness of the trend. From the figure, we notice that the charge distributions become steeper with beam energy that reflects the violence of the collisions. Similar findings are also reported in Refs. [119, 121, 243]. This behavior of charge distributions with energy is opposite to that observed with impact parameter [92, 243]. As impact parameter increases, destruction of the initial nucleon-nucleon correlations reduces and one sees large number of IMFs that turn into heavier fission-type fragments at peripheral collisions. Generally, charge distributions are fitted with a power law $\propto Z_f^{-\tau}$. We also fit these yields with power law $\propto Z_f^{-\tau}$ for intermediate mass fragments ($3 \leq Z_f \leq 12$). One notices that the present isospin-dependent quantum molecular dynamics model calculations using soft equation of state reproduce the measured charge yields nicely.

Also, to understand the behavior of the power law factor (τ) with incident energy,

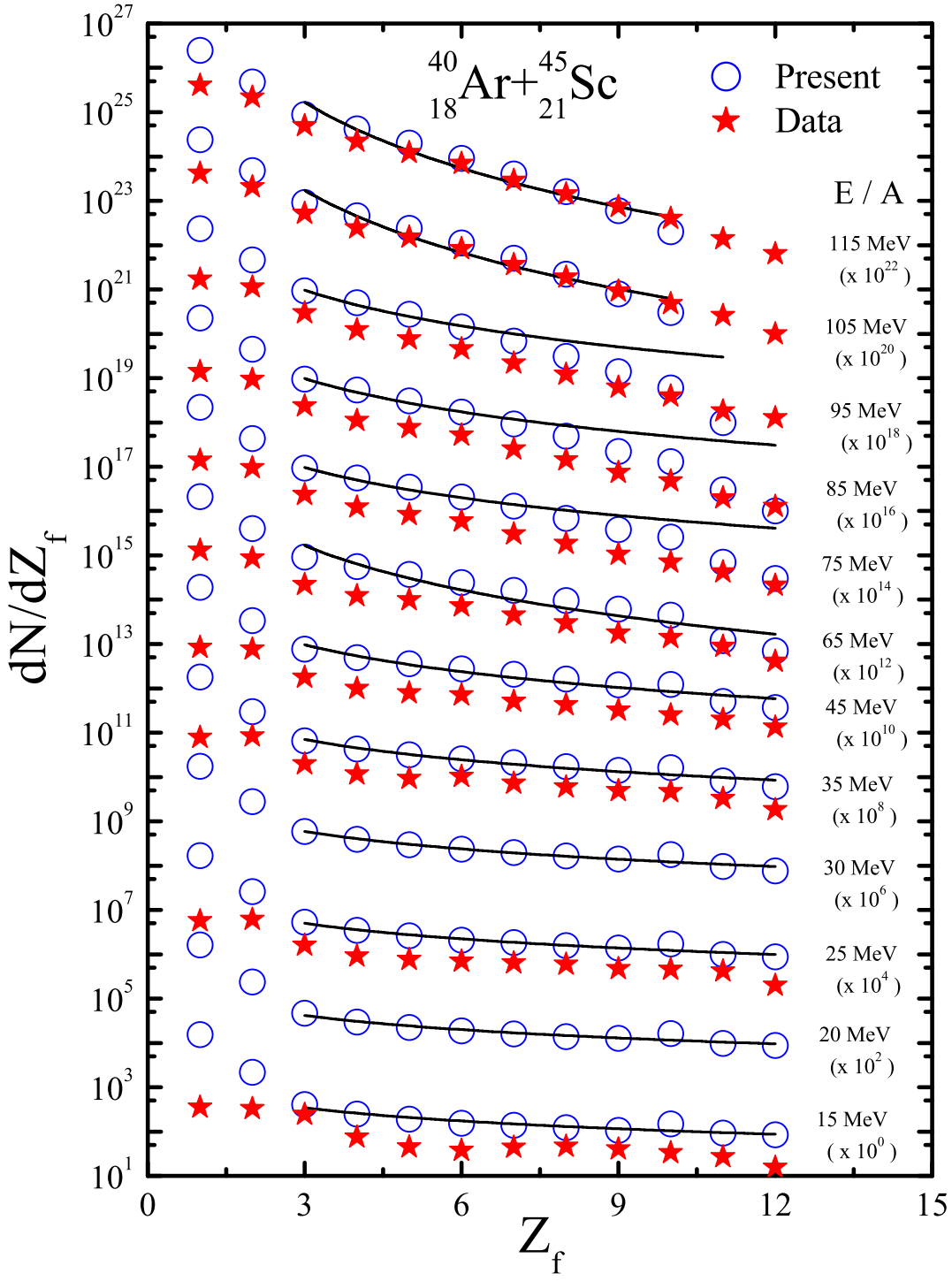

Figure 3.4: The charge distributions of the central collisions of $^{40}_{18}$Ar + $^{45}_{21}$Sc at beam energies between 15 and 115 MeV/nucleon. Open circles correspond to present calculations using soft equation of state whereas, stars represent the experimental data [121]. The solid lines represent power law fits over intermediate mass fragments ($3 \leq Z_f \leq 12$). Note that charge distributions at beam energies between 20 and 115 MeV/nucleon have been scaled by factor labeled within the figure.

we display in Fig. 3.5, extracted values of the factor τ (from Fig. 3.4) as a function of incident energy. We find that τ increases with incident energy reflecting the steepening

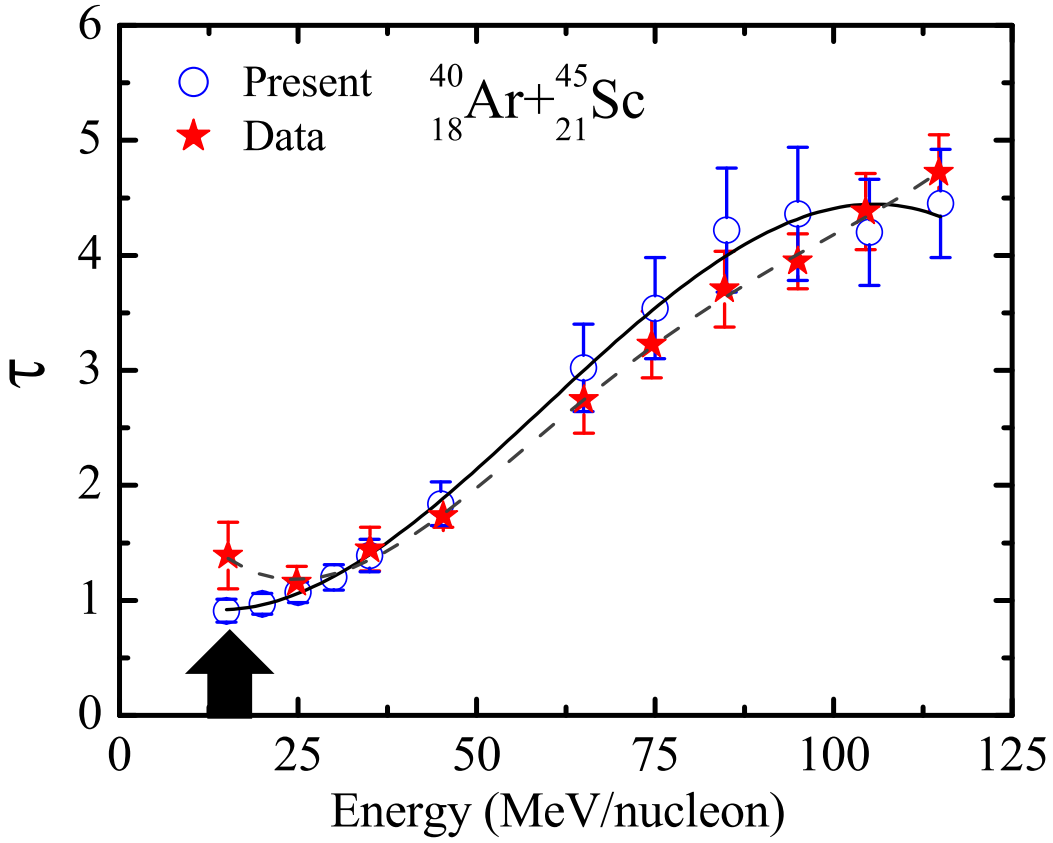

Figure 3.5: Extracted values of parameter τ from the fits as done in Fig. 3.4. Solid and dashed lines represent fourth order polynomial fits of τ values obtained using soft equation of state (present calculations) and experimentally extracted τ values, respectively [121]. Arrow corresponds to the flatness behavior. Symbols have the same meaning as in Fig. 3.4.

of the charge distributions with incident energy. We also see that our model calculations using soft equation of state reproduce nicely the values of τ in most of the cases. It should be noted that we do not observe any sharp minima till 15 MeV/nucleon; rather a flat behavior is observed which may reflect the onset of multifragmentation at still lower energies. It can be either due to unavailability of precise experimental filters or indicates lower limit for IQMD model where fission and/or shell corrections and fine

structure dominate the physics. On the other hand, repulsive Coulomb forces could also be the cause. We will discuss the onset of multifragmentation and its dependence on the Coulomb forces in details in the next chapter (i.e., Chapter 4).

In Fig. 3.6, we display the charge distributions for another nearly symmetric reaction of $^{129}_{54}$Xe + $^{120}_{50}$Sn at incident energies of 32, 39 and 45 MeV/nucleon. Open circles represent our present calculations using the IQMD model and stars correspond to the experimental data [267, 268]. The results of other dynamical model, namely, improved quantum molecular dynamics (ImQMD) model [267, 268] are also shown for comparison (triangles and diamonds). Note that in Refs. [267, 268], fragments are formed by implementing additional momentum constraint in conventional MST approach (having only spatial constraint) using the phase space available from ImQMD model [267, 268]. The results of ImQMD model have been shown for three sets of equation of state [labeled as IQ1, IQ2 and IQ3]. From the figure, we find a reasonably good agreement of our calculations with the measured charge distributions for the nearly symmetric reactions of $^{129}_{54}$Xe + $^{120}_{50}$Sn at energies around Fermi-energy domain.

In Fig. 3.7, we display the charge distribution for the reaction of $^{129}_{54}$Xe + $^{120}_{50}$Sn at beam energy of 50 MeV/nucleon. Solid histogram represents our present calculations using IQMD model and stars correspond to the experimental data [175]. The results of AMD model calculations are also displayed (dashed and dotted lines). Note that the AMD model [174] calculations (quantum branching implemented) [175] are truncated at finite time (of 300 fm/c) and decay of excited fragments is done by statistical decay code [281] based on sequential binary decay model [282]. Again, we find a reasonably good agreement between our results and measured charged distributions. This agreement between experimental measurements and IQMD model results is achieved by using basic cluster algorithm (i.e, the MST method), whereas, in most of other models, the results are presented after taking into account the secondary decay of excited fragments using GEMINI and SMM models [277, 278] to explain experimental measurements [138, 175, 240]. Let us now investigate the dynamics of asymmetric reactions.

3.3.2 Asymmetric reactions

Next, we investigate the dynamics of fragmentation in various asymmetric reactions. For this, firstly we made calculations for the highly charged asymmetric system of $^{84}_{36}$Kr + $^{197}_{79}$Au ($\eta = 0.4$). The selection of the incident energies and impact parameter is as per ex-

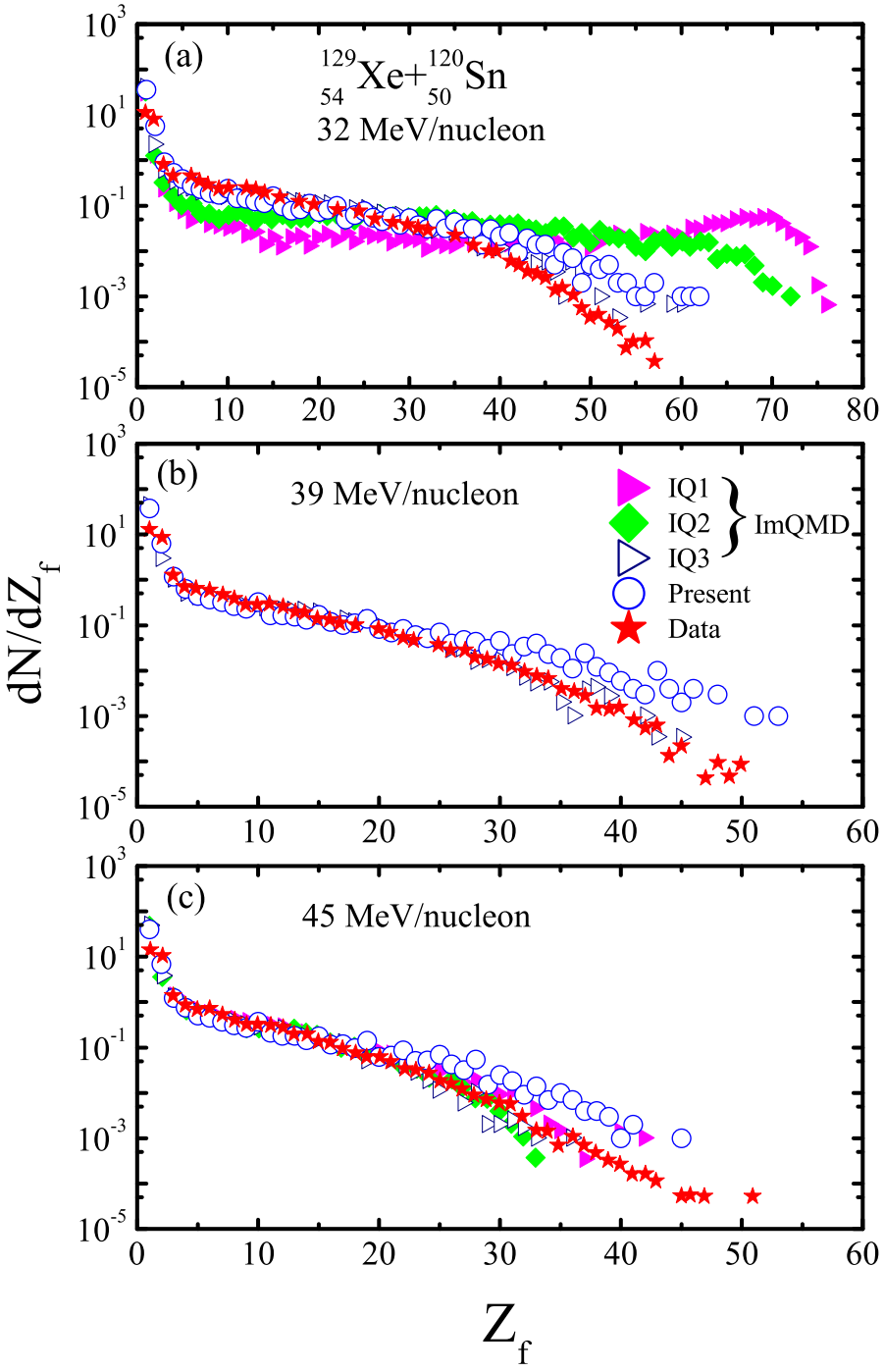

Figure 3.6: The charge distributions for the central collisions of $^{129}_{54}$Xe + $^{120}_{50}$Sn at beam energies of 32, 39 and 45 MeV/nucleon. Open circles represent our present calculations and stars correspond to experimental data [267, 268]. The other model calculations (triangles and diamonds) taken from Refs. [267, 268] are performed using ImQMD as primary model and Minimum Spanning Tree (MST) with additional momentum cut as secondary algorithm.

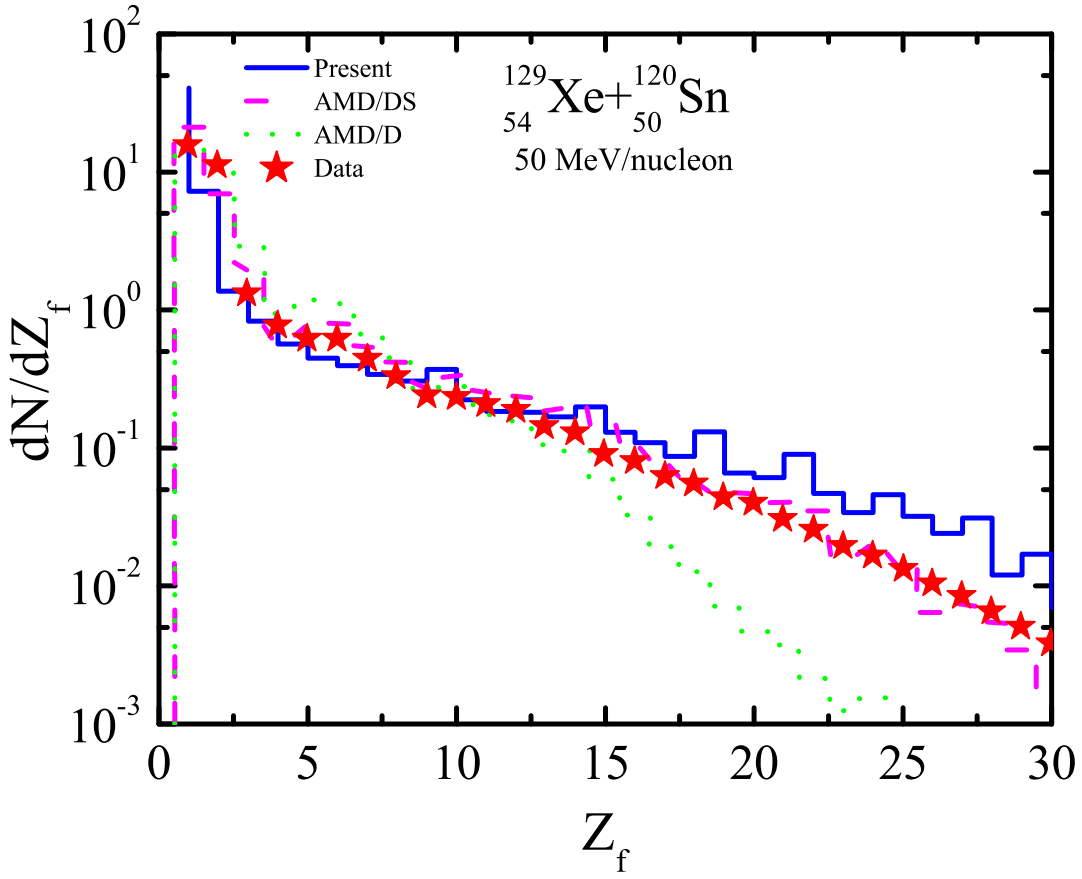

Figure 3.7: The charge distributions for the central collisions of $^{129}_{54}$Xe + $^{120}_{50}$Sn at beam energy of 50 MeV/nucleon. Solid histogram represents our present calculations and stars correspond to experimental data [175]. The other model calculations (dashed and dotted lines) taken from Ref. [175] are performed using AMD model as primary model followed by statistical decay code as secondary algorithm.

perimental measurements [122, 138]. In Fig. 3.8, the calculated charge yields ($3 \leq Z_f \leq 12$) are plotted against experimental ones. From the figure, we find that our calculated charge yields show nice agreement at lower incident energies. On the other hand, calculations deviate from the measured yield as one moves to higher incident energies. Here, calculations predict higher yield of the fragments compared to that observed experimentally. This indicates that as incident energy rises above the Fermi-domain, the IQMD model with MST clusterization technique starts deviating from the experimental data. Similar results are also observed for the symmetric reaction of $^{197}_{79}$Au + $^{197}_{79}$Au at 400 MeV/nucleon in Ref. [283] where ALADiN measurements are compared with IQMD model calculations. At the same time, nice agreement of our calculations with experimental data at lower beam energies is because of the higher Fermi-momentum in the present IQMD model that provides enough repulsion leading in enhanced emission of the IMFs.

Further, to compare our present IQMD model calculations with earlier attempts using QMD model (and afterburners) in Fig. 3.9(a), we display the multiplicities of the intermediate mass fragments, $<N_{IMFs}>$ as a function of incident energy. The shaded region corresponds to IMFs mass window between $5 \leq A_f \leq 43$ and $6 \leq A_f \leq 43$. As stated earlier, this choice of IMFs mass range is governed by experimental measurements [138]. The previously calculated results (represented by different lines) along with experimental data [138] (stars) are also shown. Whereas the QMD model with Pauli potential fails to reproduce the multiplicity of the intermediate mass fragments for present asymmetric colliding system of $^{84}_{36}$Kr + $^{197}_{79}$Au at lower incident energies [138], our present IQMD model calculations nicely reproduce the intermediate mass fragments multiplicity at lower energies (E < 100 MeV/nucleon). The close agreement of the present calculations with experimental data happens due to higher Fermi-momentum in the IQMD model compared to that in the QMD model. Note that in IQMD model, the Fermi-momentum is determined from the ground state density $\rho_0 = 0.17$ fm^{-3} (calculated from Fermi-gas model) and has a value of $\sim$ 268 MeV/c. On the other hand, the Fermi-momentum in the QMD model is limited by local binding energy in order to keep all nucleons bound [189]. The average Fermi-momentum in the QMD model is about 150-160 MeV/c. In the absence of any local constraints to evaluate Fermi-momentum in IQMD model, the nucleons closer to surface are unbound initially. It is worth mentioning here that we have calculated the binding energies of various nuclei taken in the present study. For example, the nuclei of $^{12}_{6}$C and $^{16}_{8}$O have binding energies (averaged over hundreds of stable runs)

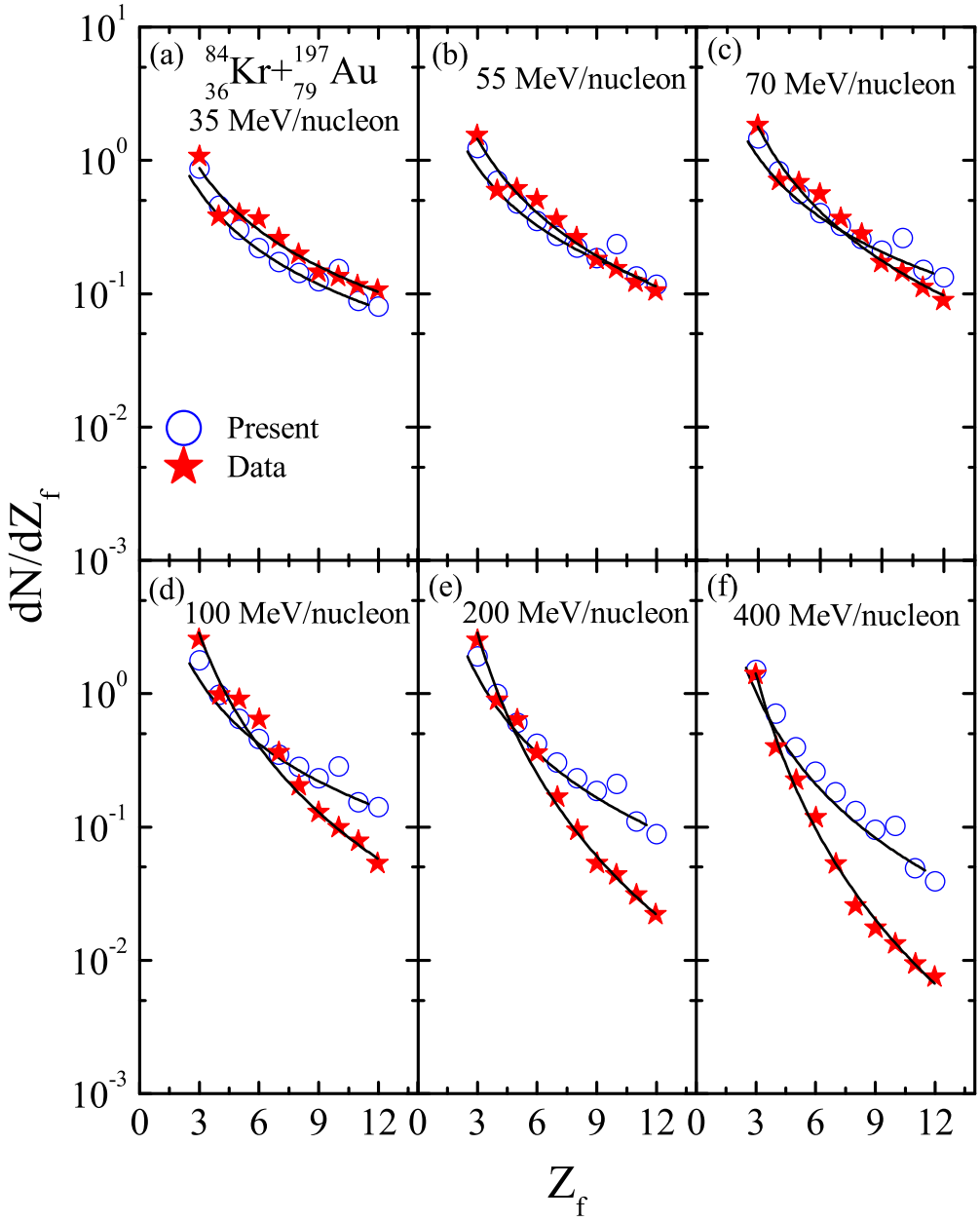

Figure 3.8: The charge distributions obtained for the central collisions of $^{84}_{36}$Kr + $^{197}_{79}$Au at beam energies between 35 and 400 MeV/nucleon. The open circles and stars correspond to the theoretical and experimental results, respectively [122]. The solid lines represent the power law fits over intermediate mass fragments ($3 \leq Z_f \leq 12$).

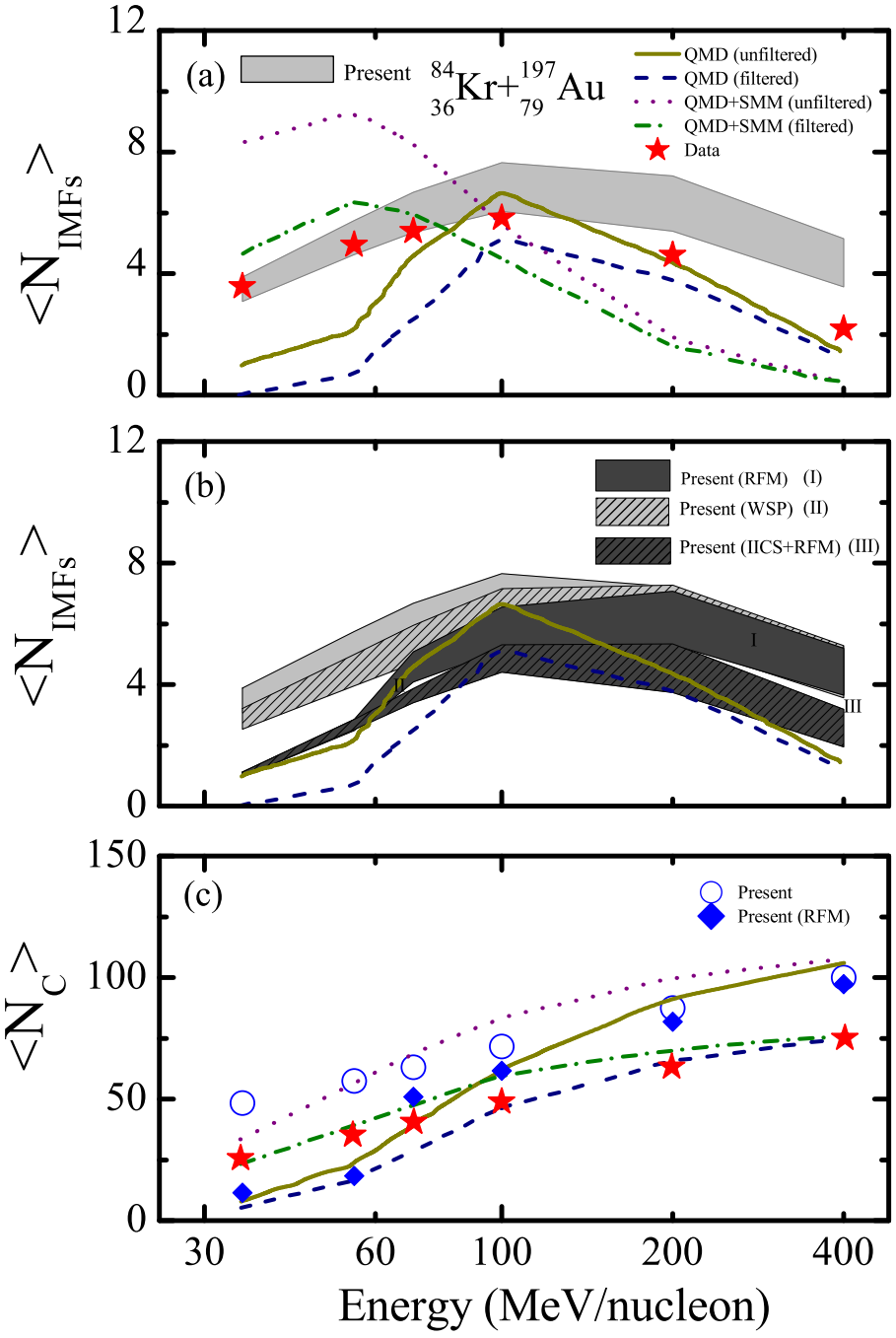

Figure 3.9: (a and b) The multiplicities of intermediate mass fragments (IMFs) and (c) of charged particles obtained in the reaction of $^{84}_{36}$Kr + $^{197}_{79}$Au. The present calculations are shown by light shaded region (a and b) and open circles (c). The dark shaded area (diamonds) represent our calculations with reduced Fermi-momentum (RFM) for $<N_{IMFs}>$ ($<N_C>$). The light crossed area represents the present calculations without symmetry potential (WSP). The calculations with reduced Fermi- momentum and isospin independent cross-section (IICS+RFM) are shown as dark crossed area. Results from other model calculations are also shown for comparison [138]. The stars correspond to experimental data extracted from Ref. [138].

of -3 to -4 MeV/nucleon whereas, the binding energies of heavier nuclei such as $^{40}_{18}$Ar, $^{45}_{21}$Sc, $^{64}_{29}$Cu, $^{84}_{36}$Kr, $^{108}_{47}$Ag, $^{120}_{50}$Sn, $^{129}_{54}$Xe and $^{197}_{79}$Au are between -4 to -5 MeV/nucleon. Note that stability fluctuations due to these improper binding energies have been balanced by introducing stable density distributions and good energy conservation. The stable density profiles have been chosen by introducing system size-dependent interaction range. The interaction range (L) for various nuclei ranges from 4.33 fm^2 to 8.66 fm^2. In particular, the interaction range for $^{45}_{21}$Sc, $^{64}_{29}$Cu, $^{80}_{35}$Br, $^{108}_{47}$Ag, $^{129}_{54}$Xe and $^{197}_{79}$Au nuclei reads as 4.50 fm^2, 5.02 fm^2, 5.46 fm^2, 6.24 fm^2, 6.75 fm^2 and 8.66 fm^2, respectively. Note that, in mass asymmetric reactions, we choose the interaction range of heavier nucleus over lighter one assuming that heavier nucleus will have dominance of the potential. This is in contrary to that implemented in QMD model where interaction range is system independent. Also in the QMD model, the proper binding energy has been achieved at the cost of large dynamical fluctuation in the initial state. Therefore, the higher Fermi-momentum in the IQMD model enhances the production of the IMFs and thus, overcomes the failure of the quantum molecular dynamics approach at lower energies. To strengthen our point, we performed calculations with reduced Fermi-momentum (by 40%, which now becomes approximately equal to that used in the QMD model). The results are displayed in Fig. 3.9(b) and are shown by dark shaded region [labeled by RFM]. We notice that with this reduced value of the Fermi-momentum, multiplicity of IMFs decreases (by approximately 50-70%) at lower incident energies but remains same at higher incident energies. Now, the results with reduced Fermi- momentum are close to the ones predicted by the QMD model at low energies (E $\leq$ 100 MeV/nucleon) and thus points towards the role of the Fermi-momentum at lower beam energies. Another difference between IQMD and QMD models is the inclusion of symmetry potential in the former one. As noted, symmetry potential will add extra repulsion and can also enhance the production of the fragments at lower beam energies. To investigate this, we also perform the IQMD model calculations without taking symmetry potential into account and results are shown by light crossed area [labeled as WSP]. Our investigation reveals that now the multiplicity of the IMFs is reduced by $\sim$ 15% at lower incident energies without altering the same at higher energies. It is worth mentioning that transverse flow has also been found to be quite sensitive towards symmetry potential near Fermi energy region as predicted in Refs. [284]. Therefore, we can say that the repulsive characteristics of the symmetry potential and high Fermi-momentum alter the fragmentation dynamics (at lower beam energies) in IQMD

model compared to QMD model. On the other hand, IMFs's multiplicity at higher incident energies using IQMD model is still higher than that obtained using QMD model. To investigate this, we performed calculations using IQMD model by further taking isospin independent cross-section along with reduced Fermi-momentum and results are shown by dark crossed area [labeled as IICS + RFM]. Note that isospin independent cross-section was constructed by taking the cross-sections of np collisions equal to that of nn (or pp) collisions. We now find that the IMF's multiplicity at higher beam energies reduces (by 30-40%) due to reduced cross-section that leads to less breakage and becomes close to that predicted using the QMD model calculations. Also, it is clear from the Fig. 3.9(a) that two stage calculations using SMM with QMD model overpredict the data at lower energies and underpredict at higher energies. This is because at lower energies, an additional contribution to the fragments occurs from the heavy residue decay in SMM calculations but at higher energies evaporation of the fragments produced in the QMD stage takes place in SMM and multiplicity of the fragments thus reduces.

In Fig. 3.9(c), we display our calculations of charged particle multiplicity, $<N_c>$ as a function of incident energy (see circles). The results of other model calculations are also shown for comparison. The number of charged particles increases with beam energy indicating the violence of the collisions. We also notice that our IQMD model calculations overpredict the experimentally observed multiplicity (stars) throughout the energy range. This may be due to the inaccessibility of the complex filters in our present calculations (as we are counting multi-hit which has been omitted experimentally as stated in the Chapter 1) and these filters play quite significant role as is clear from filtered QMD and QMD+SMM calculations (see Fig. 3.9(a)). Further, we notice that charged particle multiplicities using present IQMD calculations are higher compared to QMD calculations at lower energies. This happens due to the high Fermi-momentum which leads to more disassembly at low energies and thus yields more charged particles. This becomes more clear from the IQMD results with reduced Fermi-momentum (diamonds) that are closer to the ones obtained using QMD model calculations. Also, the reduced Fermi-momentum does not alter N_c at higher energies.

In Figs. 3.10 and 3.11, we display the calculated charge yields (normalized) for the central collisions ($\hat{b}$ = 0-0.1) of $^{16}_{8}$O + $^{80}_{35}$Br ($\eta = 0.67$) and $^{16}_{8}$O + $^{108}_{47}$Ag ($\eta = 0.74$), respectively using soft equation of state at incident energies between 25 and 200 MeV/nucleon. Here also, normalization of the charge yields at central collisions has been done as per

available experimental measurements. The present calculations and the corresponding data are displayed by solid lines and histograms, respectively. From the figures, we find that our calculations nicely reproduce the measured charge distributions for highly asymmetric reactions of $^{16}_{8}$O + $^{80}_{35}$Br and $^{16}_{8}$O + $^{108}_{47}$Ag. However, discrepancies are found for highly asymmetric system of $^{16}_{8}$O + $^{108}_{47}$Ag at low energies (25 and 50 MeV/nucleon). The calculations of previous attempts [75, 203, 285] are also displayed (see crossed triangles and dashed, dash-dotted and dash double-dotted lines). These calculations involve the results of two statistical models i.e, FREESCO and Copenhagen, which describe the breakup of excited nuclear matter [75] and a dynamical approach namely, quantum molecular dynamics (QMD) model [35]. The results of statistical models are available for three incident energies of 25, 100 and 200 MeV/nucleon [75] and QMD model calculations are available for all incident energies [203, 285]. Both statistical models use measured charge distributions for the selection of input parameters (such as energy and momentum sharing coefficients for FREESCO and excitation energy in Copenhagen model). Whereas, the version of FREESCO model where the target spectator is split (labeled as FREESCO-II, see crossed triangles) gives compatible results with the experimental Z_f - distributions, the standard participant-spectator version of FREESCO (labeled as FREESCO-I, see dashed lines) and Copenhagen single source model (see dash-dotted lines) at low beam energies are inadequate to reproduce the experimental Z_f - distributions. This inadequacy has been attributed towards the lack of some kind of many-source dynamics in these models [75]. We also display the results of the charge yields for the reactions of $^{16}_{8}$O + $^{108}_{47}$Ag of quantum molecular dynamics (QMD) model calculations [203, 285] using soft equation of state and observed that the measured yields couldn't be reproduced. However, the present calculations using IQMD model reasonably reproduces the charge distributions for asymmetric reactions. This nice agreement (using soft equation of state), in contradiction to earlier results obtained using QMD model, may be due to the additional repulsion present in terms of symmetry potential, isospin-dependent nucleon-nucleon cross-section and high Fermi-momentum. This also refutes the apprehension raised earlier [249] that molecular dynamics model may not properly treat the thermodynamical properties. At lower energy tail (25 and 50 MeV/nucleon) of $^{16}_{8}$O + $^{108}_{47}$Ag reaction, the IQMD model (and most of other models) gives more intermediate mass fragments whereas, experimentally one sees fission-type yield followed by the emission of lighter clusters. This can be taken as a lower limit of the IQMD type model (for asymmetric reactions), which does not have

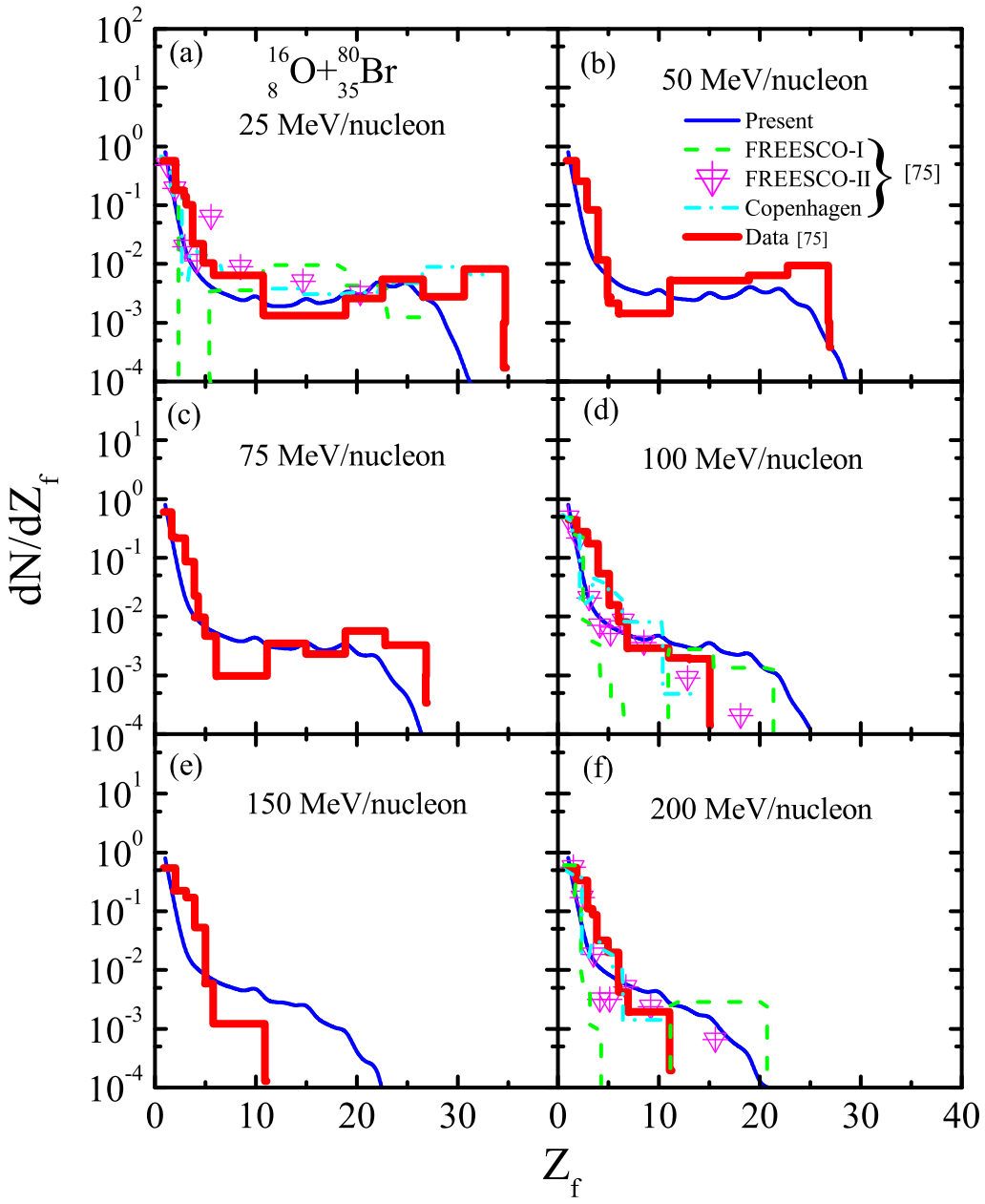

Figure 3.10: The normalized charge distributions for the reaction of $^{16}_{8}$O + $^{80}_{35}$Br at incident energies between 25 and 200 MeV/nucleon. The histograms and solid lines represent the experimental observations [75] and present IQMD calculations, respectively. The results of previous attempts [75] are also displayed for comparison.

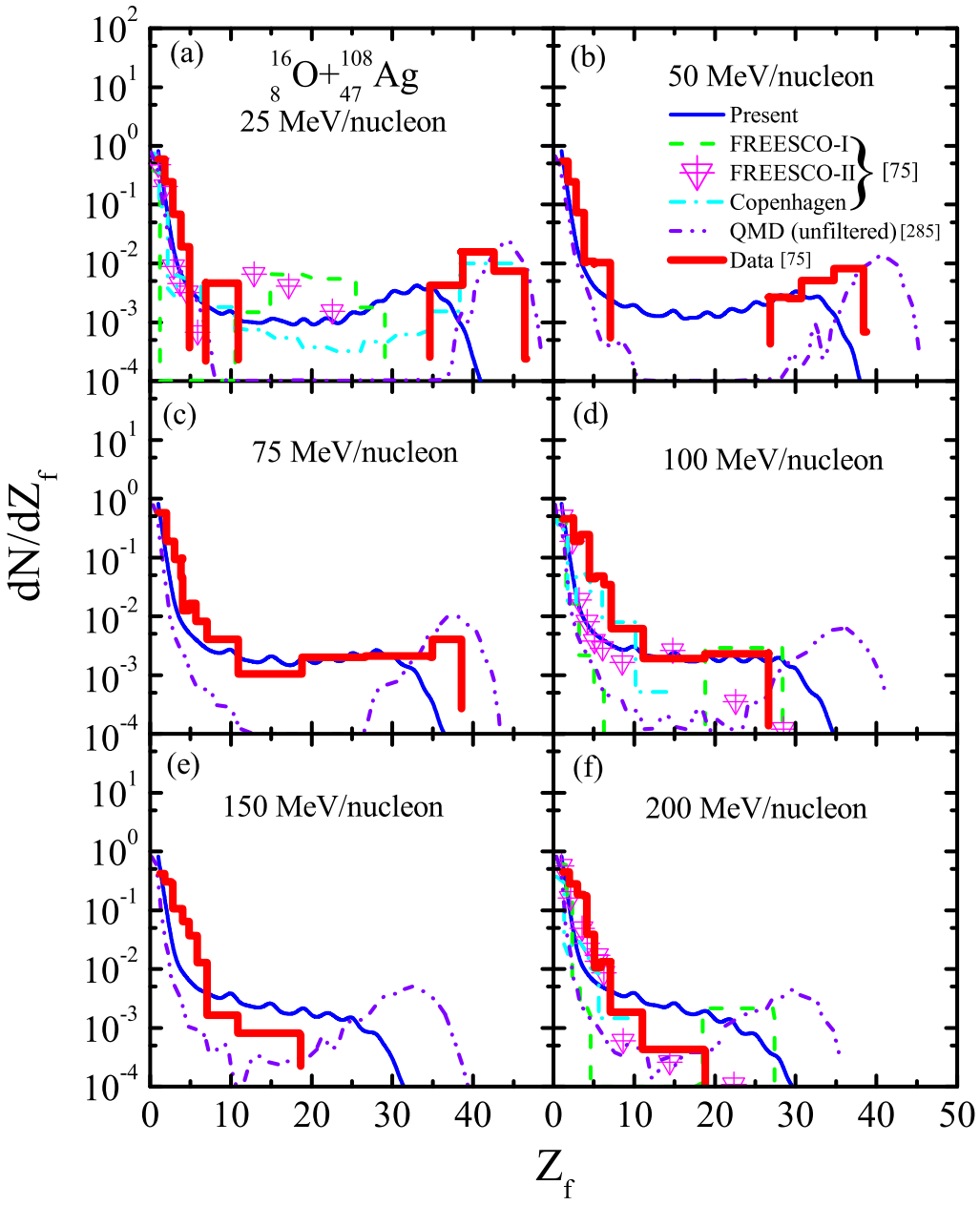

Figure 3.11: Same as Fig. 3.10, but for the reaction of $^{16}_{8}$O + $^{108}_{47}$Ag.

shell/fine structure effects in the model. It is worth mentioning that the statistical model calculations (such as FREESCO and Copenhagen) in Ref. [75] reported the inadequacy of such models to reproduce the experimental Z_f - distributions.

Next, in Fig. 3.12, calculated charge distributions for the semi-central collisions ($\hat{b}$ = 0.1-0.3) of $^{16}_{8}$O + $^{80}_{35}$Br and $^{16}_{8}$O + $^{108}_{47}$Ag are shown at incident energy of 200 MeV/nucleon. One finds that semi-cental colliding geometry leads to less violent collisions when compared with most central collisions (see Figs. 3.10 and 3.11) and this modification in the colliding geometry leads to extended tail towards higher Z_f - value. Again, results of present calculations reproduce the experimental Z_f - distributions nicely.

In Fig. 3.13, we display the charge yields for the reactions of $^{197}_{79}$Au + $^{12}_{6}$C ($\eta = 0.89$) and $^{197}_{79}$Au + $^{64}_{29}$Cu ($\eta = 0.51$) at incident energies of 25 and 35 MeV/nucleon, calculated using soft equation of state (open circles). The corresponding experimental measurements [266] are displayed by stars. Here also, a good agreement is observed between our calculations and experimentally obtained charge yields for the asymmetric collision of $^{197}_{79}$Au + $^{64}_{29}$Cu at incident energies of 25 and 35 MeV/nucleon. But for highly asymmetric reaction of $^{197}_{79}$Au + $^{12}_{6}$C at 25 MeV/nucleon, discrepancy between theoretical and experimental results can be seen. Such disagreement is also observed for highly asymmetric collision of $^{16}_{8}$O + $^{108}_{47}$Ag (see Fig. 3.11) at low energies. This may be due to the additional repulsion in IQMD model which breaks the target/projectile residues into fragments. The results of previous attempts [266] using GEMINI and SMM calculations are also shown by dashed and solid lines, respectively. The experimental charge distribution for the reaction of $^{197}_{79}$Au + $^{12}_{6}$C is well reproduced by the GEMINI model and the SMM calculations nicely reproduce the measured charge distributions for the reaction $^{197}_{79}$Au + $^{64}_{29}$Cu. The nice agreement of the GEMINI model calculations for the reaction $^{197}_{79}$Au + $^{12}_{6}$C is attributed to its features in which fragment production occurs as a sequence of binary fission-like emissions [266].

In Fig. 3.14, we display the charge distributions for the asymmetric collisions of $^{129}_{54}$Xe + $^{197}_{79}$Au ($\eta = 0.2$) and $^{40}_{18}$Ar + $^{197}_{79}$Au ($\eta = 0.66$) at incident energies of 50, 80 and 110 MeV/nucleon using soft equation of state. From the figure, we observe that our calculations using soft EOS are in nice agreement with the experimental measurements. Earlier calculations performed using Percolation model [94] are also displayed (see dash-dotted and dotted lines for unfiltered and filtered calculations, respectively for bond breaking probability P = 0.7). A slightly higher multiplicity of IMFs is though obtained at higher beam energies in accordance with earlier results (as in Fig. 3.9). As we see from Percola-

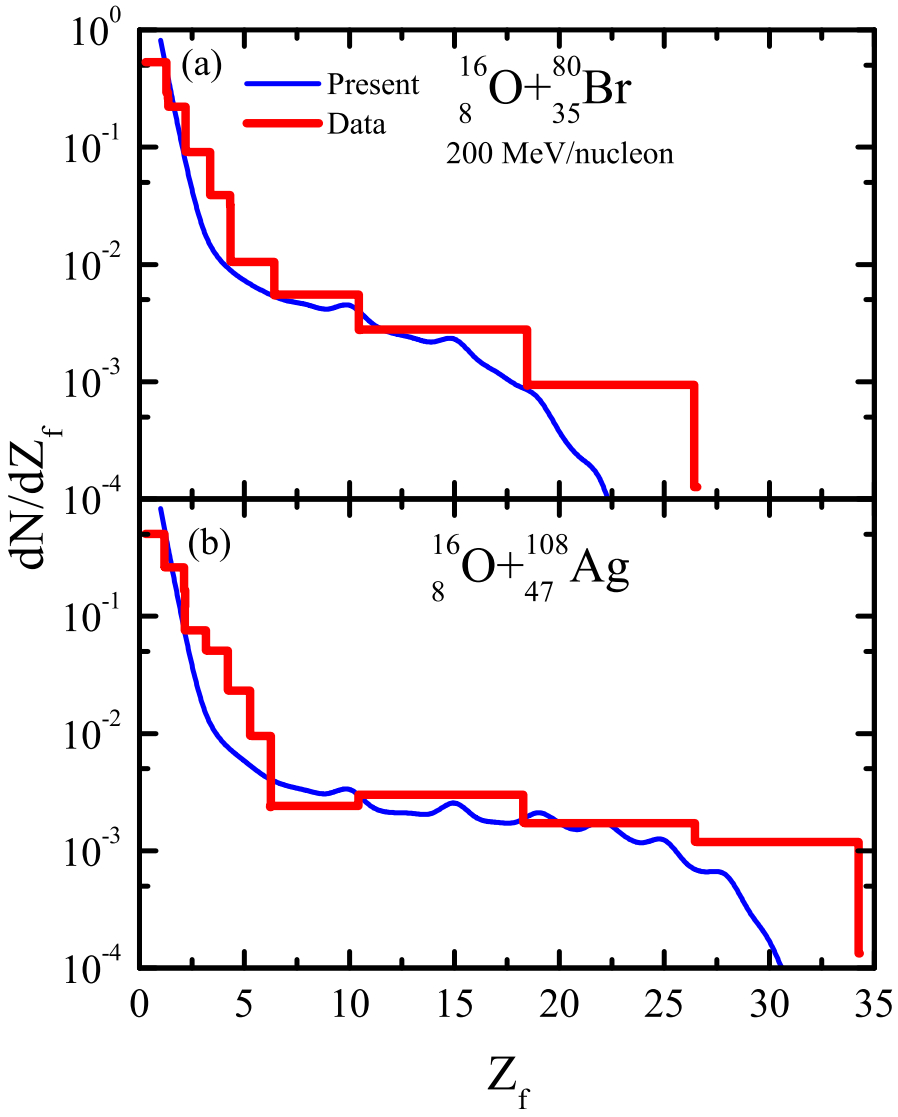

Figure 3.12: The normalized charge distributions for the reactions of $^{16}_{8}$O + $^{80}_{35}$Br and $^{16}_{8}$O + $^{108}_{47}$Ag at semi-central ($\hat{b} = 0.1$-0.3) colliding geometry. The lines have the same meaning as in Fig. 3.10 and data is extracted from Ref. [75].

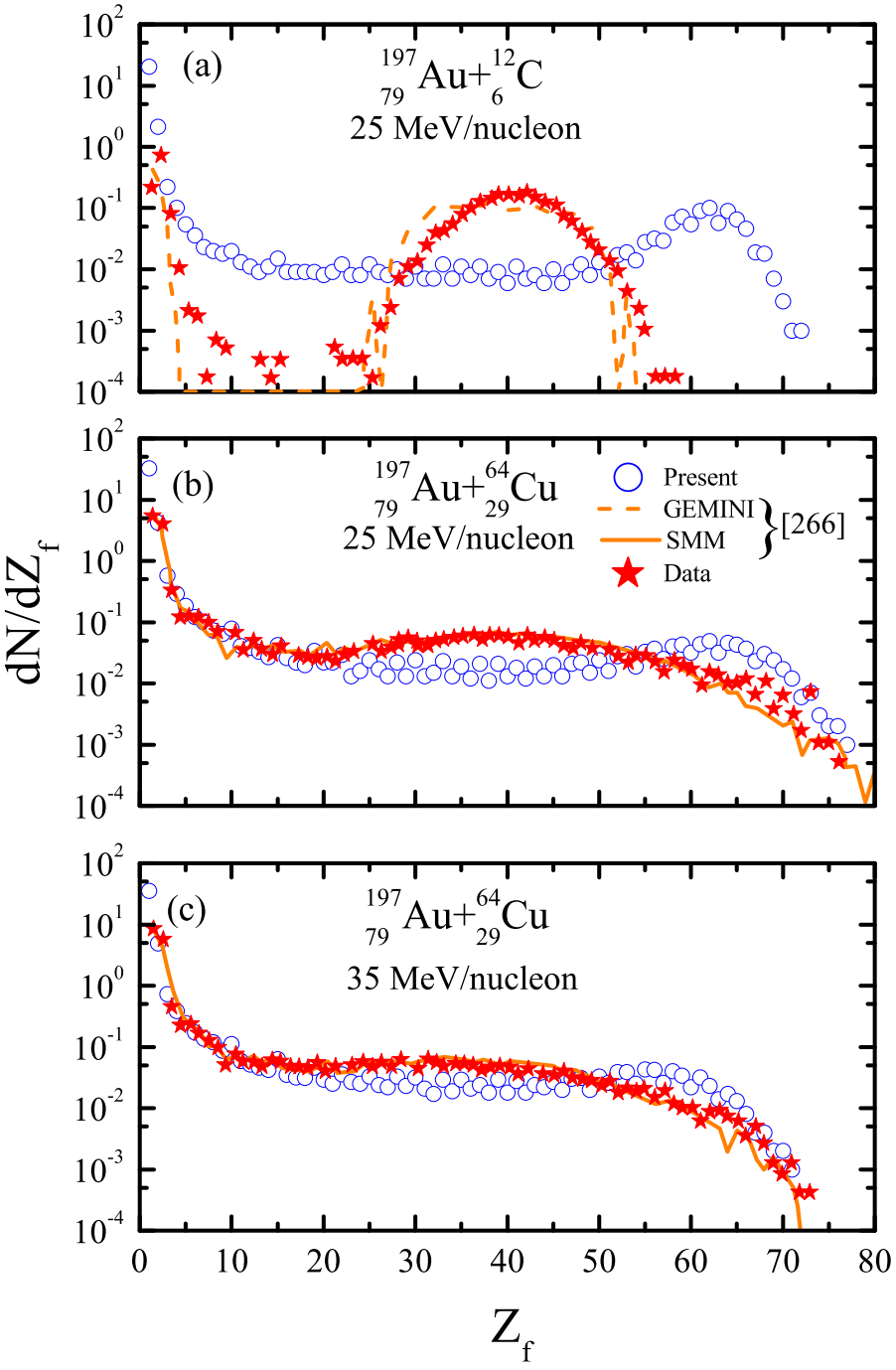

Figure 3.13: The charge distributions for the reaction of $^{197}_{79}$Au + $^{12}_{6}$C at 25 MeV/nucleon and $^{197}_{79}$Au + $^{64}_{29}$Cu at 25 and 35 MeV/nucleon, respectively. Experimental data and previous results are taken from Ref. [266].

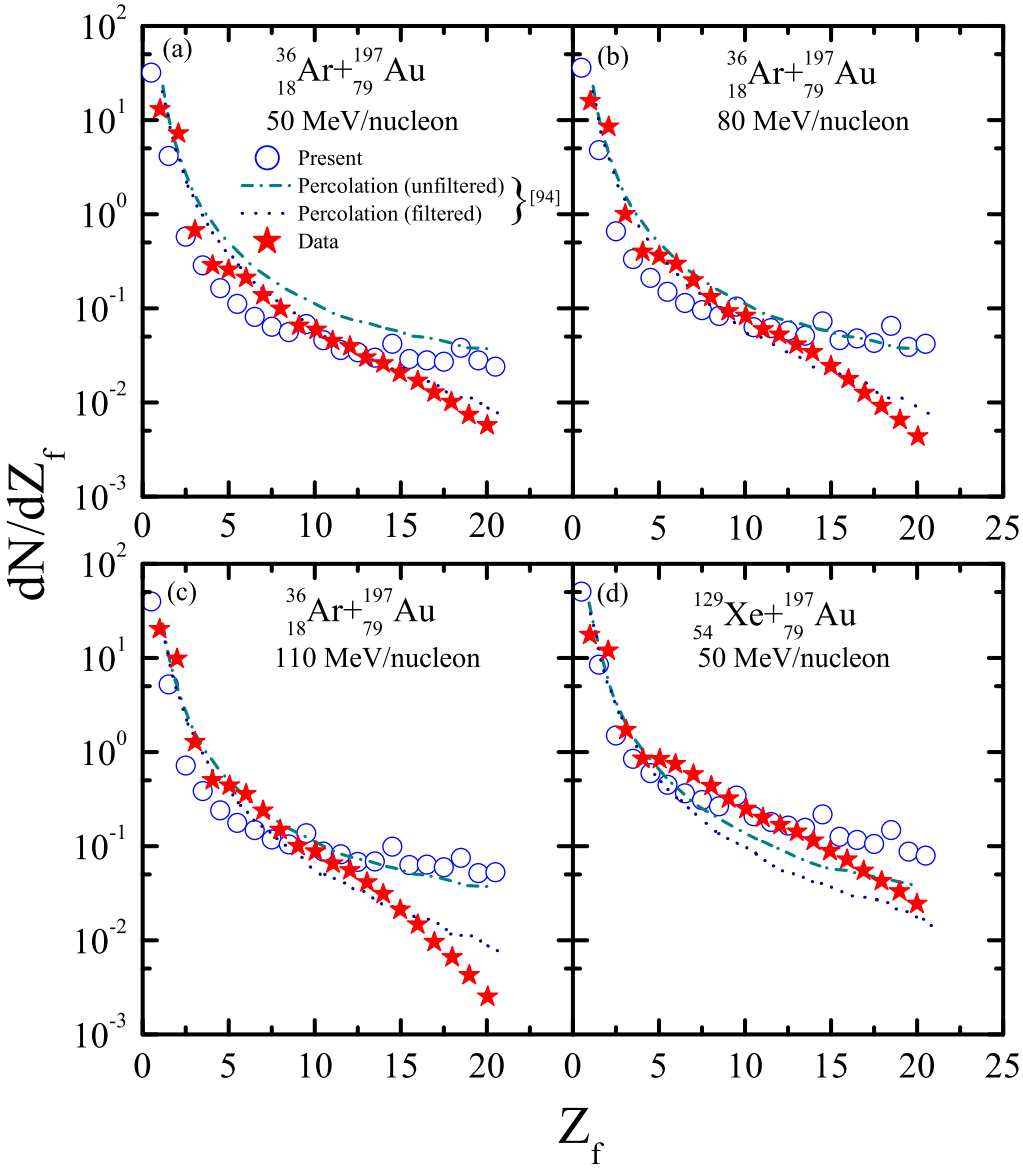

Figure 3.14: The charge distributions for the reactions of $^{36}_{18}$Ar + $^{197}_{79}$Au at incident energies of 50, 80 and 110 MeV/nucleon and $^{129}_{54}$Xe + $^{197}_{79}$Au at 50 MeV/nucleon, respectively. Experimental data is taken from Ref. [94]. The different lines correspond to the results of previous attempts [94].

tion calculations, after filtering the results of our calculations can also yield closer results. In Fig. 3.15, we display the size of heaviest fragment $<A_f^{max}>$ (top panels), multiplicities

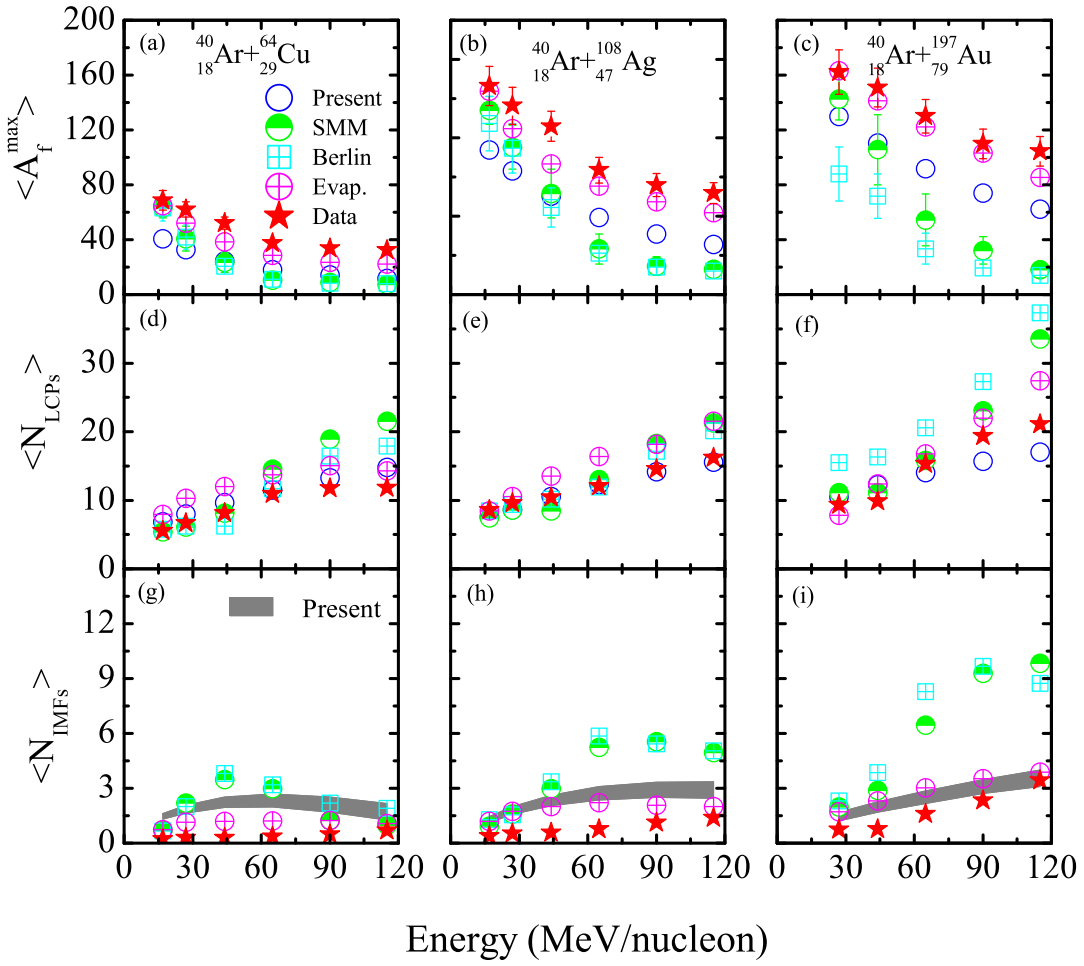

Figure 3.15: Average mass of heaviest fragment $<A_f^{max}>$ (top panel), multiplicities of light charged particles $<N_{LCPs}>$ (middle) and intermediate mass fragments $<N_{IMFs}>$ (bottom) as a function of incident energy for the central collisions of $^{40}_{18}$Ar + $^{64}_{29}$Cu, $^{40}_{18}$Ar + $^{108}_{47}$Ag and $^{40}_{18}$Ar + $^{197}_{79}$Au. Experimental data and other model calculations are taken from Ref. [97].

of the light charged particles $<N_{LCPs}>$ (middle panels) and intermediate mass fragments $<N_{IMFs}>$ (bottom panels) for the reactions of $^{40}_{18}$Ar + $^{64}_{29}$Cu (η = 0.23), $^{40}_{18}$Ar + $^{108}_{47}$Ag (η = 0.46) and $^{40}_{18}$Ar + $^{197}_{79}$Au (η = 0.66) as a function of incident energy. Open circles and stars represent our present calculations and experimental data [97], respectively. The calculated multiplicity of IMFs is represented by shaded area (corresponding to mass window between $5 \leq A_f \leq 38$ and $6 \leq A_f \leq 38$, chosen as per experimental data). The results of previous attempt [97] using SMM (half filled circles), Berlin (crossed squares) and Evaporation (crossed circles) models are also displayed. From the figure, we find that our present calculations yield smaller $<A_f^{max}>$ because of extra repulsion in terms of symmetry potential, Fermi-momentum and isospin dependence of nucleon-nucleon cross-section. Similar results are also obtained using SMM and Berlin model which also invest much energy in nuclear disassembly and bond breakage compared to the Evaporation model. This yields higher multiplicities of intermediate mass fragments using our present and former two model calculations. On the other hand, the Evaporation model shares more energy in terms of kinetic energy of ejectiles (and less in nuclear breaking) and thus yields bigger $<A_f^{max}>$. We find that our calculations reasonably reproduce the experimental results.

3.4 Summary

We presented an extensive analysis of various symmetric as well as asymmetric reactions (asymmetry parameter η varying between 0.2 and 0.89) using a dynamical model, namely isospin-dependent quantum molecular dynamics model and compared our calculations with available experimental data. Our study revealed that the IQMD model nicely explains the dynamics of asymmetric reactions at energies around Fermi-energy domain. At extreme low incident energies (where fission fragments and/or fine structure dominates), the calculations with IQMD model can be seen to deviate. Similarly, at higher incident energies (say $\geq$400 MeV/nucleon), the calculations with IQMD model again show certain deviation. We also carried out a detailed comparison with various other model calculations (wherever available). Our detailed analysis revealed that the inclusion of symmetry potential, isospin-dependent nucleon-nucleon cross-section and high Fermi-momentum in IQMD model can handle the difficulties reported in reproducing results with quantum molecular dynamics approach.